

Phases of hot nuclear matter at subnuclear densities

Genaro Watanabe^{a,b,c}, Katsuhiko Sato^{a,d}, Kenji Yasuoka^e and Toshikazu Ebisuzaki^b

^a*Department of Physics, University of Tokyo, Tokyo 113-0033, Japan*

^b*Computational Astrophysics Laboratory, RIKEN, Saitama 351-0198, Japan*

^c*NORDITA, Blegdamsvej 17, DK-2100 Copenhagen Ø, Denmark*

^d*Research Center for the Early Universe, University of Tokyo, Tokyo 113-0033, Japan*

^e*Department of Mechanical Engineering, Keio University, Yokohama 223-8522, Japan*

(Dated: February 9, 2020)

Structure of hot dense matter at subnuclear densities is investigated by quantum molecular dynamics (QMD) simulations. We analyze nucleon distributions and nuclear shapes using two-point correlation functions and Minkowski functionals to determine the phase-separation line and to classify the phase of nuclear matter in terms of the nuclear structure. Obtained phase diagrams show that the density of the phase boundaries between the different nuclear structures decreases with increasing temperature due to the thermal expansion of nuclear matter region. The critical temperature for the phase separation is $\gtrsim 6$ MeV for $x = 0.5$ and $\gtrsim 5$ MeV for $x = 0.3$. Our result suggests the existence of “spongelike” phases with negative Euler characteristic in addition to the simple “pasta” phases in supernova cores until $T \lesssim 3$ MeV.

PACS numbers: 21.65.+f, 26.50.+x, 97.60.Bw, 61.20.Ja

I. INTRODUCTION

In the process of the collapse-driven supernova [1], matter in the core experiences adiabatic compression: the central density increases from $\sim 10^9$ g cm⁻³ at the beginning of the collapse to around the normal nuclear density $\rho_0 = 0.165$ fm⁻³ just before bounce; the temperature reaches $\sim O(1)$ MeV at this point.

At subnuclear densities, nuclear matter exhibits the coexistence of a liquid phase with a gas phase due to the internucleon interaction which has an attractive part. In the density region where nuclei are about to melt into uniform matter, it is expected that, at sufficiently low temperatures relevant to neutron star interiors [2], the energetically favorable configuration of the mixed phase possesses interesting spatial structures such as rodlike and slablike nuclei and rodlike and spherical bubbles, etc., which are referred to as nuclear “pasta” [3, 4].

This prediction is confirmed by several approaches assuming nuclear shapes such as the liquid drop models [5, 6, 7] and the Thomas-Fermi calculations [8], and is also confirmed without assuming nuclear shapes in the framework of the Thomas-Fermi approximation [9] and of the quantum molecular dynamics (QMD) [10, 11]. While nuclear pasta at zero temperature is studied by several authors, pasta phases at finite temperatures relevant to supernova inner cores have not been studied yet except for a work by Lassaut et al. using the Thomas-Fermi approximation [12] and brief estimates of thermal fluctuations of the long-wave-length mode [6, 7]. It is noted that, at temperatures of several MeV, effects of thermal fluctuations on nucleon distribution would be quite significant at subnuclear densities. However, the mean-field approximation such as the Thomas-Fermi [13] and Hartree-Fock [14] approximation is not suitable to incorporate thermal fluctuations.

Finite temperature effects lead to evaporation of nu-

cleons from nuclear liquid region and smoothed nucleon density profiles. At lower temperatures where each nuclei fluctuates a little around an average species, a compressible liquid-drop model [15] with incorporating the temperature dependence of its bulk, surface, and Coulomb+lattice components provides a useful way to investigate the pasta phases at finite temperatures. As for the bulk component [16], binding energy, saturation density, and incompressibility [17], which are parameters characterizing saturation properties, decrease with increasing temperature while the temperature dependence of the symmetry energy is not significant [18]. For surface component, thermal broadening of the nucleon density profile reduces nuclear surface tension [19]. Lattice energy is also modified by translational motion of nuclei [15]. However, at higher temperatures where the fluctuation of nuclear shape is significant, the above liquid-drop picture no longer holds; we have to call on some ab-initio method which does not assume nuclear shape. More interestingly, it might be possible that, at these temperatures, the shape of the nuclear surface fluctuates and nuclei of various sizes and shapes coexist like colloid due to the entropy effect.

These finite temperature effects can be well described by the methods of molecular dynamics (MD) for nucleon many-body systems (see, e.g., Ref. [20] for review). QMD [21], which is one of them, enables us to treat much larger systems than the other methods of MD do. Furthermore, at temperatures of several MeV, shell effects, which cannot be incorporated by QMD, are less important because they washed away by thermal fluctuations above ~ 3 MeV.

Pasta phases in supernova matter (SNM) are expected to affect the neutrino transport and hydrodynamics in supernova cores. Let us first note that the neutrino wavelengths, typically of order 20 fm, are comparable to or even greater than the internuclear spacing, lead-

ing to diffractive effects on the neutrino elastic scattering off such a periodic spatial structure of nuclear matter [3]. These effects, induced by the internuclear Coulombic correlations, would reduce the scattering rates and hence the lepton fraction Y_L . For the bcc lattice of spherical nuclei, such a reduction was examined by Horowitz [22] by calculating the associated static structure factor. It is also noteworthy that nonspherical nuclei and bubbles are elongated in specific direction. In such direction, the neutrino scattering processes are no longer coherent, in contrast to the case of roughly spherical nuclei whose finiteness in any direction yields constructive interference in the scattering, which leads to the neutrino-trapping [23, 24]. The final point to be mentioned is that the changes in the nuclear shape are accompanied by discontinuities in the adiabatic index, denoting how hard the equation of state of the material is. These discontinuities may influence the core hydrodynamics during the initial phase of the collapse [12].

In the present paper, we study the structure of hot dense matter at subnuclear densities within the framework of QMD. Simulations of nuclear matter with proton fraction $x = 0.3$ in addition to symmetric nuclear matter ($x = 0.5$) are performed because the typical value of the proton fraction for supernova matter is around 0.3 due to the trapping of the electron neutrinos [23, 24]. We draw phase diagrams for $x = 0.5$ and 0.3 in the density versus temperature plane, which show the qualitative feature of the finite temperature effects on the structure of nuclear matter. The results of the present study would be helpful to understand the real situation of the interior of the collapsing cores.

The plan of this paper is as follows. In Section II, we briefly explain the QMD model used in the present study and then discuss an effective temperature. In this

section, a thermostatting method used in the simulations is also explained. In Section III, we show snapshots of some typical nucleon distributions to discuss qualitative features of finite temperature effect. After that, we analyze the structure of matter using two-point correlation functions and Minkowski functionals, and finally, resultant phase diagrams are shown. Summary and conclusion are presented in Section IV.

II. FORMULATION

A. Model Hamiltonian

Simulating nuclear matter at subnuclear densities within the framework of QMD, we use a QMD model Hamiltonian developed by Maruyama et al. [26], which is constructed so as to reproduce bulk properties of nuclear matter and properties of finite nuclei. This model Hamiltonian, which describes interactions between nucleons, consists of the following six terms

$$\mathcal{H} = T + V_{\text{Pauli}} + V_{\text{Skyrme}} + V_{\text{sym}} + V_{\text{MD}} + V_{\text{Coulomb}} , \quad (1)$$

where T is the kinetic energy, V_{Pauli} is the Pauli potential introduced to reproduce the Pauli principle effectively, V_{Skyrme} is the Skyrme potential which consists of an attractive two-body term and a repulsive three-body term, V_{sym} is the symmetry potential, V_{MD} is the momentum-dependent potential introduced as two Fock terms of the Yukawa interaction and V_{Coulomb} is the Coulomb energy including the constant contribution V_{p-e} due to the Coulomb interaction between protons and electrons [27]. The expressions of these terms are given as

$$T = \sum_{i,j(\neq i)} \frac{\mathbf{P}_i^2}{2m_i} , \quad (2)$$

$$V_{\text{Pauli}} = \frac{1}{2} C_P \left(\frac{\hbar}{q_0 p_0} \right)^3 \sum_{i,j(\neq i)} \exp \left[-\frac{(\mathbf{R}_i - \mathbf{R}_j)^2}{2q_0^2} - \frac{(\mathbf{P}_i - \mathbf{P}_j)^2}{2p_0^2} \right] \delta_{\tau_i \tau_j} \delta_{\sigma_i \sigma_j} , \quad (3)$$

$$V_{\text{Skyrme}} = \frac{\alpha}{2\rho_0} \sum_{i,j(\neq i)} \rho_{ij} + \frac{\beta}{(1+\tau)\rho_0^\tau} \sum_i \left[\sum_{j(\neq i)} \int d^3\mathbf{r} \tilde{\rho}_i(\mathbf{r}) \tilde{\rho}_j(\mathbf{r}) \right]^\tau , \quad (4)$$

$$V_{\text{sym}} = \frac{C_s}{2\rho_0} \sum_{i,j(\neq i)} (1 - 2|c_i - c_j|) \rho_{ij} , \quad (5)$$

$$\begin{aligned} V_{\text{MD}} &= V_{\text{MD}}^{(1)} + V_{\text{MD}}^{(2)} \\ &= \frac{C_{\text{ex}}^{(1)}}{2\rho_0} \sum_{i,j(\neq i)} \frac{1}{1 + \left[\frac{\mathbf{P}_i - \mathbf{P}_j}{\hbar\mu_1} \right]^2} \rho_{ij} + \frac{C_{\text{ex}}^{(2)}}{2\rho_0} \sum_{i,j(\neq i)} \frac{1}{1 + \left[\frac{\mathbf{P}_i - \mathbf{P}_j}{\hbar\mu_2} \right]^2} \rho_{ij} , \end{aligned} \quad (6)$$

$$V_{\text{Coulomb}} = \frac{e^2}{2} \sum_{i,j(\neq i)} \left(\tau_i + \frac{1}{2} \right) \left(\tau_j + \frac{1}{2} \right) \iint d^3\mathbf{r} d^3\mathbf{r}' \frac{1}{|\mathbf{r} - \mathbf{r}'|} \rho_i(\mathbf{r}) \rho_j(\mathbf{r}') + V_{p-e} , \quad (7)$$

where ρ_{ij} means the overlap between the single-nucleon densities, $\rho_i(\mathbf{r})$ and $\rho_j(\mathbf{r})$, for i -th and j -th nucleons given as

$$\rho_{ij} \equiv \int d^3\mathbf{r} \rho_i(\mathbf{r}) \rho_j(\mathbf{r}), \quad (8)$$

σ_i is the nucleon spin and τ_i is the isospin ($\tau_i = 1/2$ for protons and $-1/2$ for neutrons) and C_P , q_0 , p_0 , α , β , τ , C_s , $C_{\text{ex}}^{(1)}$, $C_{\text{ex}}^{(2)}$, μ_1 , μ_2 and L are model parameters determined to reproduce the properties of the ground states of the finite nuclei, especially heavier ones, and the saturation properties of nuclear matter [26]. A parameter set used in this work is shown in Table I. The single-nucleon densities $\rho_i(\mathbf{r})$ and $\tilde{\rho}_i(\mathbf{r})$ are given as

$$\rho_i(\mathbf{r}) = |\phi_i(\mathbf{r})|^2 = \frac{1}{(2\pi L)^{3/2}} \exp\left[-\frac{(\mathbf{r} - \mathbf{R}_i)^2}{2L}\right], \quad (9)$$

$$\tilde{\rho}_i(\mathbf{r}) = \frac{1}{(2\pi \tilde{L})^{3/2}} \exp\left[-\frac{(\mathbf{r} - \mathbf{R}_i)^2}{2\tilde{L}}\right], \quad (10)$$

with

$$\tilde{L} = \frac{(1 + \tau)^{1/\tau}}{2} L. \quad (11)$$

The quantity $\tilde{\rho}_i(\mathbf{r})$ is introduced in the three body term of Skyrme interaction Eq. (4) to incorporate the effect of the repulsive density-dependent term by the modified width \tilde{L}

TABLE I: Effective interaction parameter set ($K=280$ MeV; medium EOS model in Ref. [26])

α (MeV)	-92.86
β (MeV)	169.28
τ	1.33333
C_s (MeV)	25.0
$C_{\text{ex}}^{(1)}$ (MeV)	-258.54
$C_{\text{ex}}^{(2)}$ (MeV)	375.6
μ_1 (MeV)	2.35
μ_2 (MeV)	0.4
L (fm ²)	2.1

B. Effective temperature

The effective Hamiltonian (1) used in this work contains momentum dependent interactions, i.e. the Pauli potential V_{Pauli} and the momentum dependent potential V_{MD} . Thus the usual expression for the instantaneous kinetic temperature T_{kin} given as

$$\frac{3}{2}k_B T_{\text{kin}} = \frac{1}{N} \sum_{i=1}^N \frac{\mathbf{P}_i^2}{2m_i}, \quad (12)$$

loses its meaning of the temperature in thermodynamics. We here use an effective temperature T_{eff} proposed by Chikazumi et al. [28], which is given as

$$\begin{aligned} \frac{3}{2}k_B T_{\text{eff}} &= \frac{1}{N} \sum_{i=1}^N \frac{1}{2} \mathbf{P}_i \cdot \frac{d\mathbf{R}_i}{dt} \\ &= \frac{1}{N} \sum_{i=1}^N \frac{1}{2} \mathbf{P}_i \cdot \left(\frac{\partial \mathcal{H}}{\partial \mathbf{P}_i} \right). \end{aligned} \quad (13)$$

It can be immediately seen that this expression is equivalent to the usual kinetic temperature defined by Eq. (12) if the effective Hamiltonian \mathcal{H} does not have momentum dependent interactions (i.e., V_{Pauli} and V_{MD}).

In order to confirm whether the effective temperature T_{eff} is consistent with temperature in the Boltzmann statistics, we perform Metropolis Monte Carlo (MC) simulations [29, 30, 31] with 256 nucleons (with $x = 0.5$, i.e., 128 protons and 128 neutrons). We investigate six given temperatures $T_{\text{set}} = 0.1, 1, 3, 5, 7$ and 10 MeV at four nucleon densities $\rho = 0.1, 0.3, 0.5$ and $0.8 \rho_0$ within a wide region of the phase diagram at subnuclear densities covering from a phase-separating region to a uniform fluid region. We prepare a cubic box, which is imposed of the periodic boundary condition. In the simulations the system is equilibrated at a given temperature T_{set} for 1000 MC steps (i.e. $1000 \times N$ trial moves), and then sampling is carried out for the following 10000 MC steps. Sampled values of the instantaneous effective temperature T_{eff} is plotted in Fig. 1. We can see from this figure that the instantaneous effective temperature T_{eff} fluctuates around the given value of T_{set} . It is noted that the long-time averaged values $\langle T_{\text{eff}} \rangle$ of the effective temperature coincide with T_{set} quite well within the fluctuations of order $\sim T_{\text{set}}/\sqrt{N}$ due to the finite particle number. Thus we can conclude that the effective temperature given by Eq. (13) is consistent with temperature in the Boltzmann statistics. It is also confirmed that, in microcanonical molecular dynamics simulations, the mean value of the effective temperature keeps constant after the system is equilibrated enough.

The instantaneous effective temperature can be negative as plotted in Fig. 1 for $T_{\text{set}} = 0.1$ when \mathbf{P}_i and $\dot{\mathbf{R}}_i$ take the opposite directions each other due to the contribution of the momentum dependent interactions. However, it is also confirmed that, after the system is relaxed, the long-time average of the effective temperature does not take negative values when we pursue the time evolution of the system by the QMD equations of motion even though some friction terms were attached to them like Eqs. (17) in Ref. [11]. In the remaining part of this paper, we measure temperature T by the effective temperature.

FIG. 1: Sampled values of the instantaneous effective temperature T_{eff} and their long-time averages $\langle T_{\text{eff}} \rangle$ for $\rho = 0.1, 0.3, 0.5$ and $0.8 \rho_0$. (This figure is included separately in JPEG format.)

C. Thermostat

It is necessary to perform “isothermal” QMD simulations in order to equilibrate the system at a specified effective temperature. In ordinary molecular dynamics simulations, what is called the Nosé-Hoover thermostat is commonly used to carry out constant-temperature simulations [30, 31, 32, 33]. The approach of Nosé and Hoover is based on the Hamiltonian of an extended system, which contains additional and artificial coordinates and velocities intended to mimic the dynamics of the system in contact with a thermal bath. It is shown by Nosé that this method generates the states in the canonical ensemble average, i.e., the microcanonical ensemble average in the extended system reduces to the canonical ensemble average in the real system. For example, the momentum distribution coincides with the Maxwell-Boltzmann distribution exactly after the system is well equilibrated with this thermostat.

Here we modify the Nosé-Hoover’s method so as to adapt to the effective temperature. The Hamiltonian of the extended system in this case can be written as

$$\begin{aligned} \mathcal{H}_{\text{Nosé}} &= \sum_{i=1}^N \frac{\mathbf{P}_i^2}{2m_i} + \mathcal{U}(\{\mathbf{R}_i\}, \{\mathbf{P}_i\}) + \frac{sp_s^2}{2Q} + g \frac{\ln s}{\beta} \\ &= \mathcal{H} + \frac{sp_s^2}{2Q} + g \frac{\ln s}{\beta}, \end{aligned} \quad (14)$$

where $\mathcal{U}(\{\mathbf{R}_i\}, \{\mathbf{P}_i\})$ is the potential which depends on both positions and momenta, s is the additional dynamical variable for time scaling, p_s is the momentum conjugate to s , Q is the thermal inertial parameter corresponding to a coupling constant between the system and thermostat [in our simulations, we set $Q \sim 10^8 \text{ MeV} (\text{fm}/c)^2$], g is a parameter to be determined as $3N$ by a condition for generating the canonical ensemble in the classical molecular dynamics simulations, and β is defined as $\beta \equiv 1/k_B T_{\text{set}}$. The equations of motion yield

$$\frac{d\mathbf{R}_i}{dt} = \frac{\partial \mathcal{H}_{\text{Nosé}}}{\partial \mathbf{P}_i} = \frac{\mathbf{P}_i}{m_i} + \frac{\partial \mathcal{U}}{\partial \mathbf{P}_i}, \quad (15)$$

$$\frac{d\mathbf{P}_i}{dt} = -\frac{\partial \mathcal{H}_{\text{Nosé}}}{\partial \mathbf{R}_i} = -\frac{\partial \mathcal{U}}{\partial \mathbf{R}_i} - \xi \mathbf{P}_i, \quad (16)$$

$$\frac{1}{s} \frac{ds}{dt} = \frac{1}{s} \frac{\partial \mathcal{H}_{\text{Nosé}}}{\partial p_s} = \frac{1}{Q} \frac{\partial \mathcal{H}_{\text{Nosé}}}{\partial \xi} = \xi, \quad (17)$$

$$\frac{d\xi}{dt} = \frac{1}{Q} \left\{ \sum_{i=1}^N \left(\frac{\mathbf{P}_i^2}{m_i} + \mathbf{P}_i \cdot \frac{\partial \mathcal{U}}{\partial \mathbf{P}_i} \right) - \frac{g}{\beta} \right\}, \quad (18)$$

with

$$\xi \equiv \frac{sp_s}{Q}, \quad (19)$$

where ξ means the thermodynamic friction coefficient.

In the dynamical process described by these equations, $\mathcal{H}_{\text{Nosé}}$ is conserved and the value of the effective temperature fluctuates around T_{set} as can be seen from Eq. (18).

III. SIMULATIONS AND RESULTS

A. Procedures for simulations

Let us here explain the procedure for the simulations. We investigate nuclear matter with proton fractions $x = 0.5$ and 0.3 at subnuclear densities in sufficiently wide regions of the density versus temperature plane covering the whole region where there is phase separation: symmetric nuclear matter is studied up to $\rho = 0.7\rho_0$ and $T = 8 \text{ MeV}$, and nuclear matter with $x = 0.3$, up to $\rho = 0.6\rho_0$ and $T = 7 \text{ MeV}$. Intervals of the density and the temperature between the investigated points are $0.025\rho_0$ or $0.05\rho_0$ and 0.5 MeV or 1 MeV , respectively (from the present section onward, we set $k_B = 1$).

We perform simulations for a cubic box with periodic boundary condition. We treat the (n, p, e) system with 2048 nucleons (for some typical cases of the columnar phase and the planar phase, a system with 16384 nucleons is also used). Throughout this paper, we treat systems which are not magnetically polarized, i.e. they contain equal numbers of protons (and neutrons) with spin up and spin down. The relativistic degenerate electrons which ensure charge neutrality are regarded as a uniform background because the influence of the electron screening on the phase diagram at subnuclear densities is small as shown explicitly in Ref. [25]. The Coulomb interaction is calculated by the Ewald method taking account of the Gaussian charge distribution of the proton wave packets (see, e.g., Appendix A in Ref. [11]), which enables us to sum up the contributions of long-range interactions in a system with periodic boundary conditions efficiently. For the nuclear interaction, we use the effective Hamiltonian developed by Maruyama et al. (medium EOS model) [26], the expressions for which are given in Section II A.

We first prepare a hot, uniform gas with 2048 nucleons at $T \sim 20 \text{ MeV}$ as an initial condition, which is equilibrated for $\sim 500 - 2000 \text{ fm}/c$ in advance. We then cool it down slowly for $O(10^3 - 10^4) \text{ fm}/c$ keeping the nucleon density unchanged by the frictional relaxation method [see Eqs. (17) of Ref. [11]] until the temperature reaches $\sim 5 \text{ MeV}$. For the present QMD model, this is the typical temperature for the boundary of the phase-separating region at subnuclear densities relevant to the pasta phases. In some cases, the thermostat of the Nosé-Hoover type (see Section II C) is also used to cool the system down

quickly until $\simeq 10$ MeV, at which temperature matter is still completely uniform.

After the cooling process, the system is then relaxed for $\sim 4000 - 5000$ fm/c at a given temperature T_{set} using the thermostat of the Nosé-Hoover type, which is followed by a further relaxation for ~ 5000 fm/c at the same T_{set} without the thermostat (i.e., microcanonical molecular dynamics simulation). Thermal averages are measured in the microcanonical relaxation. The above relaxation processes with and without the thermostat are repeated for the other values of T_{set} by changing T_{set} by 0.5 or 1 MeV and keeping the density constant.

Simulations of a larger system with 16384 nucleons have also been performed for some typical cases of the phases with slablike nuclei and with rodlike nuclei to examine the importance of finite size effects. We combine eight replicated samples at $T = 0$ with 2048 nucleons into a 16384-nucleon sample. We then add numerical noise to the positions and the momenta of nucleons, up to 0.1 fm in the position and 1 MeV/c in the momentum. We increase the temperature by 1 MeV and relax the system for $\sim 4000 - 5000$ fm/c using the Nosé-Hoover thermostat and relax further for $\sim 3000 - 5000$ fm/c without the thermostat. These relaxation processes are repeated for $T_{\text{set}} = 2$ and 3 MeV.

The simulations of the 2048-nucleon system are performed using PCs (Pentium III) equipped with MDGRAPE-2, and those of the 16384-nucleon system are done by Fujitsu VPP 5000 equipped with MDGRAPE-2.

B. Two-point correlation functions and Minkowski functionals

To analyze the spatial distribution of nucleons, we use the two-point correlation function. The two-point correlation function ξ_{ii} for the nucleon density field $\rho^{(i)}$ ($i = N, p, n$; where N stands for nucleons) is here defined as

$$\xi_{ii}(r) = \frac{1}{4\pi} \int d\Omega_{\mathbf{r}} \frac{1}{V} \int d^3\mathbf{x} \delta_i(\mathbf{x}) \delta_i(\mathbf{x} + \mathbf{r}) \quad (20)$$

$$\equiv \langle \delta_i(\mathbf{x}) \delta_i(\mathbf{x} + \mathbf{r}) \rangle_{\mathbf{x}, \Omega_{\mathbf{r}}}, \quad (21)$$

where $\langle \cdots \rangle_{\mathbf{x}, \Omega_{\mathbf{r}}}$ denotes an average over the position \mathbf{x} and the direction of \mathbf{r} , and $\delta_i(\mathbf{x})$ is the fluctuation of the density field $\rho^{(i)}(\mathbf{x})$ given by

$$\delta_i(\mathbf{x}) \equiv \frac{\rho^{(i)}(\mathbf{x}) - \overline{\rho^{(i)}}}{\overline{\rho^{(i)}}}, \quad (22)$$

with

$$\overline{\rho^{(i)}} \equiv \frac{N_i}{V}. \quad (23)$$

To identify the nuclear surface and extract its morphological characteristics, we use the Minkowski functionals (see, e.g., Ref. [34] and references therein; a concise review is provided by Ref. [35]; a brief explanation is given

in Section IV C of Ref. [11]), especially of the integral mean curvature and the Euler characteristic [36].

Suppose we set a threshold density ρ_{th} and consider the regions where the density is higher than this value surrounded by the isodensity surfaces for ρ_{th} (the procedure for identifying the nuclear surface, which is characterized by isodensity surfaces for a specific value of ρ_{th} , will be explained in Section III D). The integral mean curvature and the Euler characteristic are defined as surface integrals of the following local quantities: the mean curvature $H = (\kappa_1 + \kappa_2)/2$ and the Gaussian curvature $G = \kappa_1 \kappa_2$, i.e., $\int_{\partial K} H dA$ and $\chi \equiv \frac{1}{2\pi} \int_{\partial K} G dA$, where κ_1 and κ_2 are the principal curvatures and dA is the area element of the surface of the body K . The Euler characteristic χ is a purely topological quantity and is expressed as

$$\chi = (\text{number of isolated regions}) - (\text{number of tunnels}) + (\text{number of cavities}). \quad (24)$$

Here we introduce their normalized quantities: the area-averaged mean curvature, $\langle H \rangle \equiv \frac{1}{A} \int H dA$, and the Euler characteristic density, χ/V , where V is the volume of the whole space.

In the present work, we use 64^3 (128^3) grid points for the 2048-nucleon (16384-nucleon) system in constructing the nucleon density distribution $\rho^{(i)}(\mathbf{x})$. Detailed procedures for calculating ξ_{ii} ($\langle H \rangle$ and χ/V) are given in Section IV A (IV C) of Ref. [11].

C. Typical nucleon distributions for the phases with rodlike and slablike nuclei

Let us first show some snapshots of the nucleon distribution at finite temperatures for densities corresponding to the phases with slablike nuclei and with rodlike nuclei at $T = 0$. These snapshots help us to understand the qualitative feature of finite temperature effects on the nuclear structure.

Figures 2 and 3 show snapshots of the nucleon distribution for $x = 0.5$ at a density of $0.225\rho_0$ (the phase with cylindrical nuclei at $T = 0$) and Figs. 4 and 5 show ones for $x = 0.5$ and $\rho = 0.4\rho_0$ (the phase with planar nuclei at $T = 0$). Here we show snapshots of the 2048-nucleon system and those of the 16384-nucleon system for both cases. Figures 8 and 9 for $x = 0.3$ are the same as Figs. 3 and 5 for $x = 0.5$, respectively; Fig. 8 is for $0.175\rho_0$ (the phase with cylindrical nuclei at $T = 0$), and Fig. 9 is for $0.35\rho_0$ (the phase with planar nuclei at $T = 0$). The snapshots for the 16384-nucleon systems (Figs. 3, 5, 8, and 9) are depicted without perspective.

From these figures, we can see the following qualitative features irrespective of the proton fraction and the system size: at $T \simeq 1.5 - 2$ MeV (but snapshots for $T \simeq 1.5$ MeV are not shown there), the number of the evaporated nucleons starts to be significant; at $T \gtrsim 3$ MeV, the density profiles of the nucleons are smoothed out and it is difficult to identify the nuclear surface. In view of

FIG. 2: (Color) The nucleon distributions for $x = 0.5$, $\rho = 0.225\rho_0$ at the temperatures of 1,2,3 and 4 MeV. 2048 nucleons are contained in the simulation box of size $L_{\text{box}} = 38.07$ fm. These figures show the top views along the axis of the rodlike nuclei. Protons are represented by the red particles, and neutrons by the green ones. (This figure is included separately in JPEG format.)

FIG. 3: (Color) The same as Fig. 2 at the temperatures of 1,2 and 3MeV for the system with 16384 nucleons. The box size L_{box} is 76.14 fm. The upper panels show the top views along the axis of the cylindrical nuclei at $T = 0$, the lower ones the side views. (This figure is included separately in JPEG format.)

FIG. 4: (Color) The nucleon distributions for $x = 0.5$, $\rho = 0.4\rho_0$ at the temperatures of 1,2,3 and 4 MeV. 2048 nucleons are contained in the simulation box of size $L_{\text{box}} = 31.42$ fm. Protons are represented by the red particles, and neutrons by the green ones. (This figure is included separately in JPEG format.)

FIG. 5: (Color) The same as Fig. 4 at the temperatures of 1,2 and 3MeV for the system with 16384 nucleons. The box size L_{box} is 62.84 fm. These figures are shown in the direction parallel to the plane of the slablike nuclei at $T = 0$. (This figure is included separately in JPEG format.)

the fact that these general features are the same for systems with different particle number (see Figs. 2 and 3 for $\rho = 0.225\rho_0$; Figs. 4 and 5 for $\rho = 0.4\rho_0$), we can say that a qualitatively correct phase diagram can be obtained by using 2048-nucleon system. This statement is supported by the behaviors of the two-point correlation function for these two systems. It is remarkable that ξ_{NN} for the 2048-nucleon system and that for 16384-nucleon one coincide quite well, as shown in Figs. 6 and 7. However, we should note that the larger system can incorporate thermal fluctuations of longer wavelengths [37]. As can be seen by comparing Figs. 4(a) and 5(a), the slablike nuclei have waves in the 16384-nucleon system at $T = 1$ MeV, but they do not in that with 2048 nucleons.

By comparing the two cases of different values of the proton fraction in more detail, we can see that the number of the evaporated protons is significantly smaller than that of neutrons at $T \simeq 2$ MeV for $x = 0.3$ although they are close to each other at $T \simeq 2$ MeV for $x = 0.5$. Here, the number density of the evaporated neutrons is defined as the number density of neutrons outside nuclei minus that of dripped neutrons at $T = 0$. A nuclear matter region with higher proton fraction (but less than 0.5) is more energetically favorable than that with lower proton fraction because of the symmetry energy, and thus, at $x = 0.3$, neutrons are preferentially evaporated to increase the proton fraction in the nuclei.

We also note that the slablike nuclei touch and fuse with each other at $T = 2$ MeV [see Figs. 4(b) and 5(b)] while the rodlike structure persists at this temperature [see Figs. 2(b) and 3(b)]. The fragility of the phase with slablike nuclei would stem from the Landau-Peierls instability and its larger volume fraction for the nuclear matter region.

In closing the present section, we would like to mention the effect of the pressure of dripped neutrons on the

nuclear structure. For rodlike nuclei, as can be seen by comparing Figs. 3(a), (b) and 8(a), (b), because of the pressure of the dripped neutrons, they tend to elongate rather than expand in radius at $x = 0.3$ as the temperature increases, and vice versa at $x = 0.5$. The elongation of rodlike nuclei at $x = 0.3$ results in their bending [see Fig. 8(b)]. For slablike nuclei, while those at $x = 0.5$ are easy to expand in thickness and they touch with each other at $T \sim 2$ MeV, their expansion at $x = 0.3$ is smaller and they do not touch at this temperature [see Figs. 5(b) and 9(b)].

D. Phase diagrams

In constructing phase diagrams, we determine the phase separating region, identify the nuclear surface and classify the nuclear structure according to its morphological characteristics. For these purpose, we use the two-point correlation functions and the Minkowski functionals introduced in Section III B.

The phase-separation region is determined by the two-point correlation function ξ_{NN} of the nucleon density fluctuation. In Figs. 10, and 11, we plot $\xi_{NN}(r)$ for symmetric nuclear matter at $\rho = 0.225$ and $0.4\rho_0$, respectively, as typical examples. The former density corresponds to the phase with rodlike nuclei and the latter one to that with slablike nuclei at zero temperature (see Figs. 2 and 4). From these figures, we can see that the amplitude of ξ_{NN} and the relative density dispersion given by $\xi_{NN}(0)$ decrease as the temperature increases. It is also noted that the smallest value of r at which ξ_{NN} vanishes does not change much compared to the change in the amplitude. This behavior of ξ_{NN} is similar to that when the density increases keeping $T = 0$, which we have studied in detail in Ref. [11]. The important point

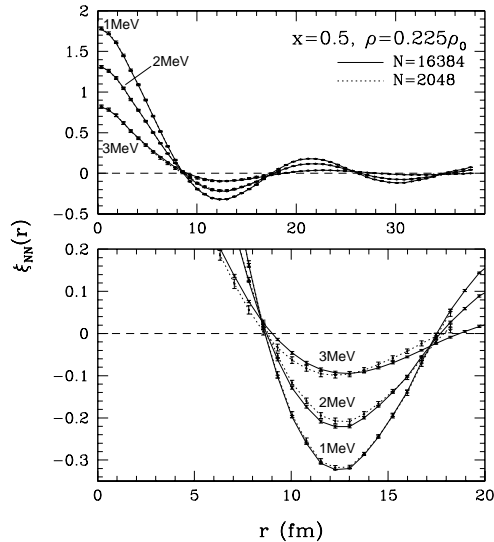


FIG. 6: Comparison of the two-point correlation functions ξ_{NN} for the systems with 2048 and 16384 nucleons. These are calculated for $x = 0.5$ and $\rho = 0.225\rho_0$, where the system is in the phase with rodlike nuclei at zero temperature. The error bars are the standard deviations in the long-time average.

is that, from the behavior of ξ_{NN} , we can determine the temperature at which the long-range correlation of the nucleon distributions disappears. Figure 10 (11) shows that the long-range correlation cannot be seen at $T = 6$ MeV (5 MeV) and thus the phase-separating boundary lies between $T = 5$ and 6 MeV at $0.225\rho_0$ ($T = 4$ and 5 MeV at $0.4\rho_0$).

The two-point correlation functions ξ_{ii} ($i = N, p$, and n) for $x = 0.3$ are also plotted in Figs. 12 and 13 for $\rho = 0.175$ and $0.35\rho_0$, respectively. As shown in Figs. 8 and 9, these densities correspond to the phases with rodlike nuclei and with slablike nuclei (Although the snapshots shown in these figures are for the 16384-nucleon system, the correlations functions ξ_{ii} shown in Figs. 12 and 13 are calculated for the 2048-nucleon system.). The amplitude of ξ_{ii} and the relative density dispersion decrease with increasing temperature as in the case of $x = 0.5$. Among ξ_{NN} , ξ_{pp} , and ξ_{nn} , the second one has the largest amplitude and the third one has the smallest except for high temperatures at which matter is almost uniform. We note that the smallest zero-points of the three kinds of ξ_{ii} almost coincide each other and they remain nearly constant at lower temperatures. This behavior shows that the density fluctuations of protons and neutrons are strongly correlated even at $x = 0.3$ and the wavelength of the density fluctuations does not change significantly at these temperatures. As can be seen from Fig. 12(a) [13(a)], the long-range correlation disappears at $T \geq 5$ MeV [$T = 4$ MeV] and thus the phase-separating boundary lies between $T = 4$ and 5 MeV at $0.175\rho_0$ [$T = 3$ and

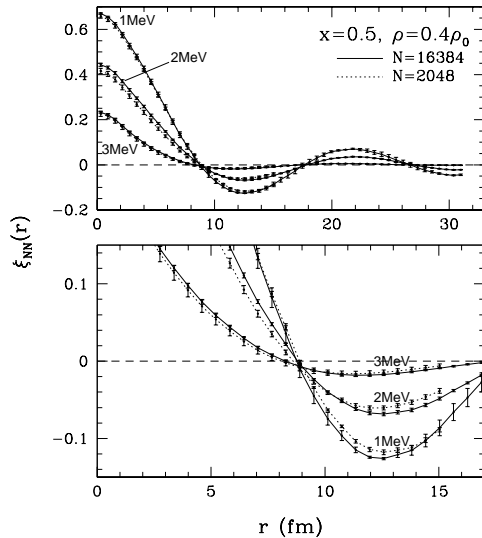


FIG. 7: The same as Fig. 6 for $x = 0.5$ and $\rho = 0.4\rho_0$, where the system is in the phase with rodlike nuclei at zero temperature.

4 MeV at $0.35\rho_0$].

To classify the phase in terms of the nuclear structure, we first have to identify nuclear surface. The Euler characteristic is useful for identifying the nuclear surface. Figures 14 and 15, show the Euler characteristic density χ/V of the nucleon density field calculated for symmetric matter for $\rho = 0.225$ and $0.4\rho_0$, respectively, and they are plotted as a function of the threshold density ρ_{th} for an isodensity surface. As for $x = 0.3$, χ/V is plotted in Figs. 16 and 17 for $\rho = 0.175$ and $0.35\rho_0$, respectively. It is noted that the curves of χ/V for lower temperatures have a plateau, which corresponds to the nuclear surface. According to these figures, the plateau of χ/V can be observed at $T = 1$ and 2 MeV, while it cannot be seen for $T \geq 3$ MeV. Thus we can say that the nuclear surface cannot be identified in the temperature range of $T \geq 3$ MeV at these values of x and ρ even in the phase-separating region. This result agrees with the qualitative feature of the snapshots of nucleon distributions shown in Figs 2 – 5, 8 and 9.

In the region where the nuclear surfaces can be identified, we sort them into several phases by their nuclear shapes. We extract morphological features of the nuclear surface using the Euler characteristic density χ/V and the averaged mean curvature $\langle H \rangle$. As one can see from Eq. (24), $\chi/V > 0$ for the sphere and the spherical hole phases, which have isolated regions and cavities, respectively (the coexistence phase of spheres and cylinders also has $\chi/V > 0$), and $\chi/V = 0$ for the other ideal pasta phases (see the plateau of $\chi/V = 0$ for lower temperatures shown in Figs. 14, 15, 16, and 17), i.e., the cylinder, the slab and the cylindrical hole phases which con-

FIG. 8: (Color) The nucleon distributions for $x = 0.3$, $\rho = 0.175\rho_0$ at the temperatures of 1, 2, and 3 MeV. 16384 nucleons are contained in the simulation box of size $L_{\text{box}} = 82.788$ fm. Protons are represented by the red particles, and neutrons by the green ones. The upper panels show the top views along the axis of the cylindrical nuclei at $T = 0$, the lower ones the side views. (This figure is included separately in JPEG format.)

FIG. 9: (Color) The nucleon distributions for $x = 0.3$, $\rho = 0.34\rho_0$ at the temperatures of 1, 2, and 3 MeV. 16384 nucleons are contained in the simulation box of size $L_{\text{box}} = 66.34$ fm. Protons are represented by the red particles, and neutrons by the green ones. These figures are shown in the direction parallel to the plane of the slablike nuclei at $T = 0$. (This figure is included separately in JPEG format.)

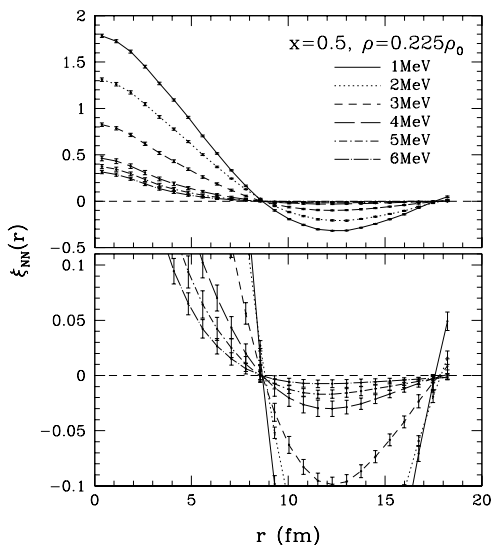


FIG. 10: Two-point correlation function of the density fluctuation calculated for $N = 2048$, $x = 0.5$ and $\rho = 0.225\rho_0$, where the system is in the phase with rodlike nuclei at zero temperature. The error bars are the standard deviations in the long-time average.

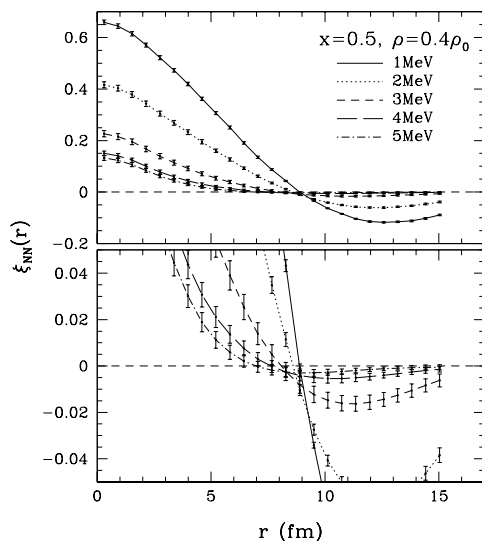


FIG. 11: Two-point correlation function of the density fluctuation calculated for $N = 2048$, $x = 0.5$ and $\rho = 0.4\rho_0$, where the system is in the phase with slablike nuclei at zero temperature. The error bars are the standard deviations in the long-time average.

sist of infinitely long rods, infinitely extending slabs and infinitely long cylindrical holes, respectively. The “spongelike” intermediate phases which are obtained in our previous works about zero-temperature matter [10, 11] have negative values of χ/V (see Fig. 12 of Ref. [11]).

As for the averaged mean curvature, at zero temperature, this quantity decreases almost monotonically from positive to negative with increasing density until matter becomes uniform (see Fig. 12 of Ref. [11]). Obviously, the zero-value of $\langle H \rangle$ corresponds to the slab phase.

In our previous work [11], the sequence of nuclear shapes at zero temperature with increasing density is described by the quantities $\langle H \rangle$ and χ/V as follows: sphere ($\langle H \rangle > 0$, $\chi/V > 0$) \rightarrow cylinder ($\langle H \rangle > 0$, $\chi/V = 0$) \rightarrow ($\langle H \rangle > 0$, $\chi/V < 0$) \rightarrow slab ($\langle H \rangle = 0$, $\chi/V = 0$) \rightarrow

($\langle H \rangle < 0$, $\chi/V < 0$) \rightarrow cylindrical hole ($\langle H \rangle < 0$, $\chi/V = 0$) \rightarrow spherical hole ($\langle H \rangle < 0$, $\chi/V > 0$) \rightarrow uniform.

Here we classify the nuclear structure at various temperatures and densities according to the combinations of signs of $\langle H \rangle$ and χ/V as we have done in the case of $T = 0$ [11]. The phase diagrams obtained for $x = 0.5$ and 0.3 are plotted in Figs. 18 and 19, respectively, in the $\rho - T$ plane [38]. Qualitative features of these phase diagrams are the same, but the phase separating-region is smaller for $x = 0.3$ than that for $x = 0.5$. As shown by dotted lines in these figures, nuclear surface can be identified typically at $T \lesssim 3$ MeV in the density range of interest. In this region where we can observe the nuclear surface, the nuclear structure changes in generally the same sequence mentioned above even at finite tempera-

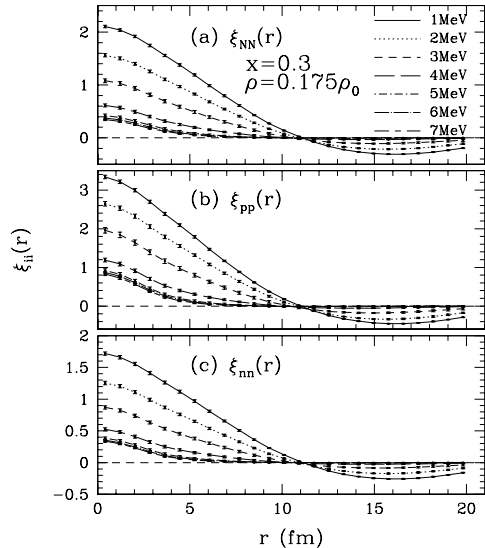


FIG. 12: Two-point correlation function of the density fluctuation calculated for $N = 2048$, $x = 0.3$ and $\rho = 0.175\rho_0$, where the system is in the phase with rodlike nuclei at zero temperature. The error bars are the standard deviations in the long-time average.

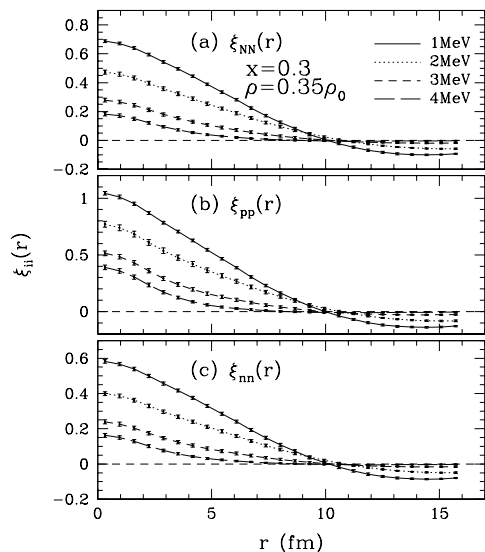


FIG. 13: Two-point correlation function of the density fluctuation calculated for $N = 2048$, $x = 0.3$ and $\rho = 0.35\rho_0$, where the system is in the phase with slablike nuclei at zero temperature. The error bars are the standard deviations in the long-time average.

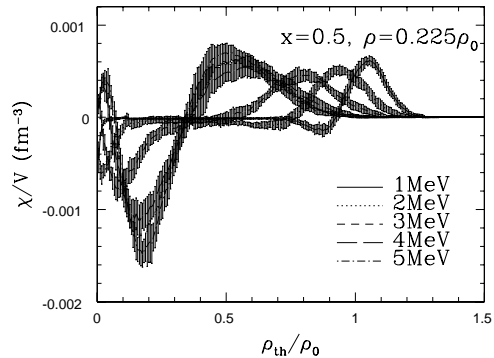


FIG. 14: Euler characteristic density for various temperatures plotted as a function of the threshold density ρ_{th} . The data shown here are calculated for $x = 0.5$ and $\rho = 0.225\rho_0$, where the system is in the phase with rodlike nuclei at zero temperature. The error bars are the standard deviations in the long-time average.

tures (the only exception is that the density region of the phase with slablike nuclei is bounded at $T \gtrsim 2$ MeV for $x = 0.3$).

The most striking finite temperature effect on the phase diagrams is that the density of each phase boundary between the different structures decreases as T increases. This is due to the thermal expansion of the nuclear matter region. At higher temperatures, the volume fraction of the nuclear matter region is larger even at smaller densities, which leads to decrease of the each phase boundary (at $0.225\rho_0$ for $x = 0.5$ and at $0.175\rho_0$ for $x = 0.3$, the volume fraction of the nuclear matter region increases by $\sim 5\%$ at $T = 2$ MeV from the value at $T = 1$ MeV; at $0.4\rho_0$ for $x = 0.5$ and at $0.35\rho_0$ for $x = 0.3$, this increase is $\sim 10 - 15\%$). This feature is less noticeable for $x = 0.3$ than $x = 0.5$, probably because the thermal expansion of nuclei is prevented by the pressure of the dripped neutrons outside of nuclei.

Above $T \sim 3$ MeV, single-particle excitations are dominant rather than collective nuclear deformation, and simultaneously, the binding potential of “nuclei” becomes smeared out. Further increase of temperature leads to dissolution of nuclei into the uniform fluid phase. The critical point for the phase separation is located at $\rho \sim 0.25\rho_0$ and $T \gtrsim 6$ MeV for $x = 0.5$ and at $\rho \sim 0.2\rho_0$ and $T \gtrsim 5$ MeV for $x = 0.3$. The above value of the critical temperature for $x = 0.5$ is not so different from the result obtained by Chikazumi et al., $T_c = 8$ MeV, using a similar nuclear potential [28].

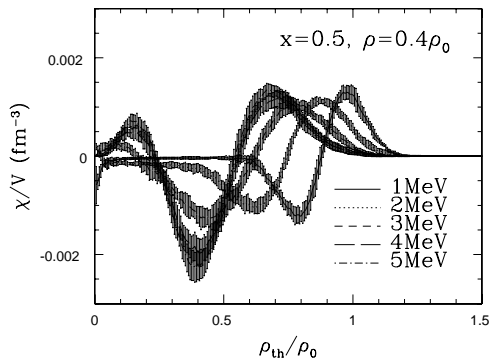


FIG. 15: The same as Fig. 14 for $\rho = 0.4\rho_0$, where the system is in the phase with slablike nuclei at zero temperature.

As far as we have investigated, the colloidal state in which nuclei of various sizes and shapes coexist cannot be observed except for the coexistence phase of spheres and cylinders. To resolve this problem, it would be necessary to perform simulations with the 16384-nucleon system for various densities other than the typical cases shown in the Section III C, or for the temperature region between 2 and 3 MeV carefully, in which the nuclear surface still remains but its fluctuations are large.

IV. SUMMARY AND CONCLUSION

We have investigated the structure of hot nuclear matter at subnuclear densities by QMD simulations. The values of the proton fraction studied in the present work are 0.5 and 0.3; the latter is a typical value in supernova inner cores. The phase diagram obtained for $x = 0.3$ (Fig. 19) tells that the pasta phases and the spongelike intermediate phases survive until $T \lesssim 3$ MeV except for the higher density region of $\rho \gtrsim 0.45\rho_0$. This result strongly suggests that these phases with exotic nuclear structures can exist in the inner cores in the pre-bounce stage of the collapse-driven supernovae. Thus it would be meaningful to investigate a modification to the neutrino opacity due to the infinitely extending “pasta” and spongelike structures in the future.

The present research has provided the general picture of the phase diagram at subnuclear densities in the temperature vs density plane. The qualitative features of the nucleon distribution at finite temperatures, except for higher densities just below which matter becomes uniform even at $T \sim 0$ MeV, may be summarized as follows.

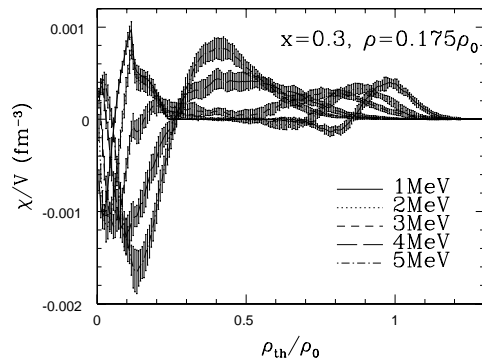


FIG. 16: Euler characteristic density for various temperatures plotted as a function of the threshold density ρ_{th} . The data shown here are calculated for $x = 0.3$ and $\rho = 0.175\rho_0$, where the system is in the phase with rodlike nuclei at zero temperature. The error bars are the standard deviations in the long-time average.

- At $T \simeq 1\text{--}1.5$ MeV, the number of evaporated nucleons starts to be significant. However, the macroscopic structure of matter does not basically change from that of zero-temperature matter except for a small expansion of the nuclear matter regions.
- At $T \simeq 1.5\text{--}2.5$ MeV, fluctuations of the nuclear shape start to be significant and, in some cases, the topology of the nuclear structure changes from that in the zero-temperature matter for the same density.
- At $T \simeq 2.5\text{--}3$ MeV, single particle excitations are dominant rather than collective excitations, representing nuclear deformations. The density profile of nucleons is smoothed out, and nuclear surface cannot be identified by a threshold density. At higher temperatures, even the density contrast becomes drastically smaller, which leads to the transition to uniform matter. The order of the transition from inhomogeneous matter to uniform matter has yet to be clarified.
- The critical temperature T_c for the phase separation is $\gtrsim 6$ MeV for $x = 0.5$ and $\gtrsim 5$ MeV for $x = 0.3$.

Through the present work and the previous ones [10, 11], we have depicted the structure of nuclear matter in neutron star inner crusts and supernova inner cores in

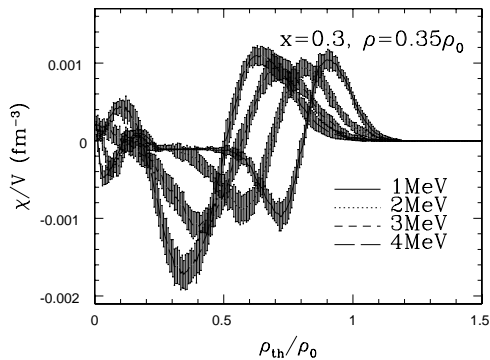


FIG. 17: The same as Fig. 16 for $0.35\rho_0$, where the system is in the phase with slablike nuclei at zero temperature.

its equilibrium state. Our studies will be helpful in understanding the realistic situations of the interior of the

dense stars. For further work, studies on the dynamical aspects of the nuclear pasta become important. For example, in connection with the possible instability of the long-range order of the planar phase, which cannot be fully incorporated in our simulations, elastic properties [39] of the pasta and spongelike phases should be studied further. Structural transitions between the pasta phases induced by compression and decompression is one of the most interesting problems which have not yet been studied at all. We believe that our work here, which was performed within a dynamical framework, will open up these new aspects of the study on nuclear pasta.

Acknowledgments

G. W. is grateful to T. Maruyama, K. Iida and I. Kayo for helpful discussions and comments. G. W. also appreciates C. J. Pethick for his valuable comments and hospitality at NORDITA and M. Shimizu, L. M. Jensen, and P. Urkedal for arranging the computer environment. This work was supported in part by the Junior Research Associate Program in RIKEN through Research Grant No. J130026 and by Grants-in-Aid for Scientific Research provided by the Ministry of Education, Culture, Sports, Science and Technology through Research Grant (S) No. 14102004, No. 14079202 and No. 14-7939.

-
- [1] H. A. Bethe, Rev. Mod. Phys. **62**, 801 (1990).
[2] C. J. Pethick and D. G. Ravenhall, Annu. Rev. Nucl. Part. Sci. **45**, 429 (1995).
[3] D. G. Ravenhall, C. J. Pethick and J. R. Wilson, Phys. Rev. Lett. **50**, 2066 (1983).
[4] M. Hashimoto, H. Seki and M. Yamada, Prog. Theor. Phys. **71**, 320 (1984).
[5] C.P. Lorenz, D.G. Ravenhall and C.J. Pethick, Phys. Rev. Lett. **70**, 379 (1993).
[6] G. Watanabe, K. Iida and K. Sato, Nucl. Phys. **A676**, 455 (2000); Nucl. Phys. **A726**, 357 (2003).
[7] G. Watanabe, K. Iida and K. Sato, Nucl. Phys. **A687**, 512 (2001); Nucl. Phys. **A726**, 357 (2003).
[8] K. Oyamatsu, Nucl. Phys. **A561**, 431 (1993).
[9] R. D. Williams and S. E. Koonin, Nucl. Phys. **A435**, 844 (1985).
[10] G. Watanabe, K. Sato, K. Yasuoka and T. Ebisuzaki, Phys. Rev. C **66**, 012801(R) (2002).
[11] G. Watanabe, K. Sato, K. Yasuoka and T. Ebisuzaki, Phys. Rev. C **68**, 035806 (nucl-th/0308007).
[12] M. Lassaut, H. Flocard, P. Bonche, P.H. Heenen and E. Suraud, Astron. Astrophys. **183**, L3 (1987).
[13] M. Barranco, J. R. Buchler, Astrophys. J. **245**, L109 (1981); Phys. Rev. C **24**, 1191 (1981).
[14] P. Bonche and D. Vautherin, Nucl. Phys. **A372**, 496 (1981).
[15] J. M. Lattimer, C. J. Pethick, D. G. Ravenhall and D. Q. Lamb, Nucl. Phys. **A432**, 646 (1985).
[16] D. Q. Lamb, J. M. Lattimer, C. J. Pethick and D. G. Ravenhall, Phys. Rev. Lett. **41**, 1623 (1978); Nucl. Phys. **A360**, 459 (1981).
[17] X. Vinas, M. Barranco, J. Treiner and S. Stringari, Astron. Astrophys. **182**, L34 (1987).
[18] P. Donati, P. M. Pizzochero, P. F. Bortignon and R. A. Broglia, Phys. Rev. Lett. **72**, 2835 (1994); D. J. Dean, K. Langanke and J. M. Sampaio, Phys. Rev. C **66**, 045802 (2002).
[19] D. G. Ravenhall, C. J. Pethick and J. M. Lattimer, Nucl. Phys. **A407**, 571 (1983).
[20] H. Feldmeier and J. Schnack, Rev. Mod. Phys. **72**, 655 (2000).
[21] J. Aichelin and H. Stöcker, Phys. Lett. **B176**, 14 (1986).
[22] C. J. Horowitz, Phys. Rev. D **55**, 4577 (1997).
[23] D. Z. Freedman, Phys. Rev. D **9**, 1389 (1974).
[24] K. Sato, Prog. Theor. Phys. **53**, 595 (1975); Prog. Theor. Phys. **54**, 1325 (1975).
[25] G. Watanabe and K. Iida, Phys. Rev. C **68**, 045801 (2003) (nucl-th/0308071).
[26] T. Maruyama, K. Niita, K. Oyamatsu, T. Maruyama, S. Chiba and A. Iwamoto, Phys. Rev. C **57**, 655 (1998).
[27] Though the term V_{p-e} in V_{Coulomb} is not explicitly written in Eq. (12) of Ref. [11], this contribution is included in the simulations in Refs. [10, 11] by the Ewald summation (see Appendix A of Ref. [11]).
[28] S. Chikazumi, T. Maruyama, S. Chiba, K. Niita and A. Iwamoto, Phys. Rev. C **63**, 024602 (2001).
[29] N. Metropolis, A. W. Rosenbluth, M. N. Rosenbluth, A. H. Teller and E. Teller, J. Chem. Phys. **21**, 1087 (1953).
[30] M. P. Allen and D. J. Tildesley, *Computer Simulation of Liquids* (Clarendon, Oxford, 1987).

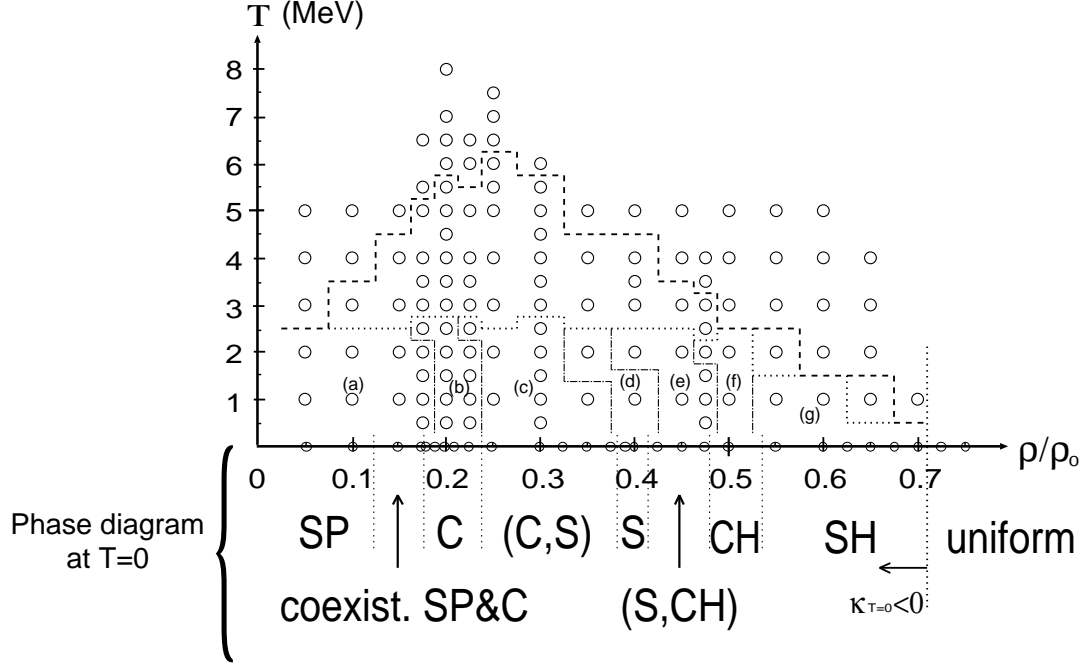


FIG. 18: Phase diagram of matter at $x = 0.5$ plotted in the $\rho - T$ plane. The dashed and the dotted lines on the diagram show the phase separation line and the limit below which the nuclear surface can be identified, respectively. The dash-dotted lines are the phase boundaries between the different nuclear shapes. The symbols SP, C, S, CH, SH, U stand for nuclear shapes, i.e. sphere, cylinder, slab, cylindrical hole, spherical hole and uniform, respectively. The parentheses (A,B) show intermediate phases between A and B-phases. The regions (a)-(g) correspond to the nuclear shapes characterized by $\langle H \rangle$ and χ/V as follows: (a) $\langle H \rangle > 0$, $\chi/V > 0$; (b) $\langle H \rangle > 0$, $\chi/V = 0$; (c) $\langle H \rangle > 0$, $\chi/V < 0$; (d) $\langle H \rangle = 0$, $\chi/V = 0$; (e) $\langle H \rangle < 0$, $\chi/V < 0$; (f) $\langle H \rangle < 0$, $\chi/V = 0$; (g) $\langle H \rangle < 0$, $\chi/V > 0$. Simulations have been carried out at points denoted by circles.

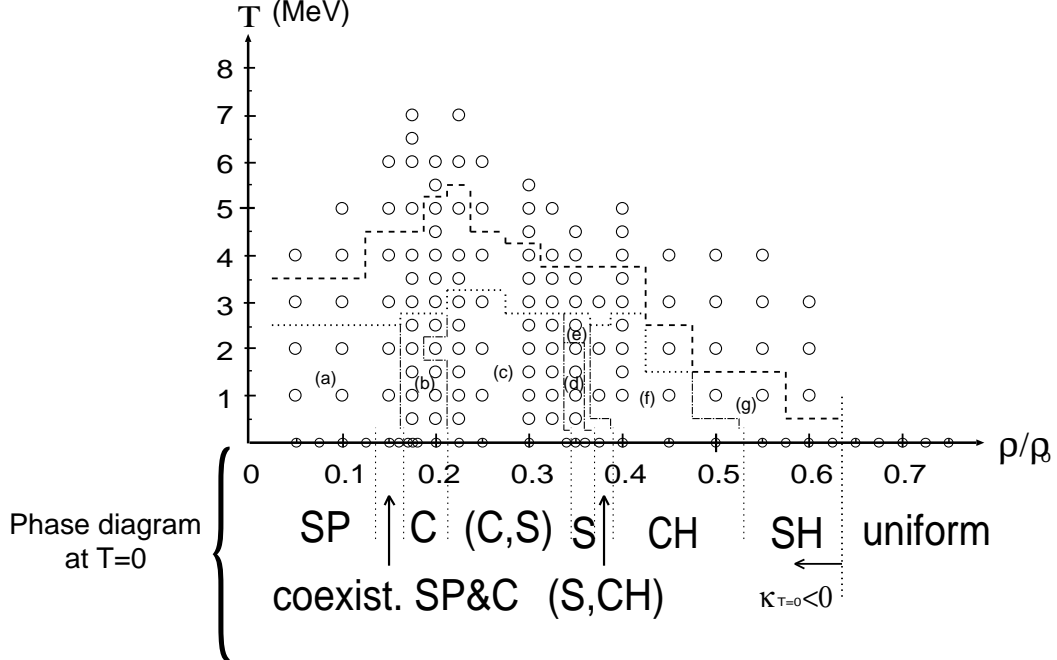


FIG. 19: Phase diagram of matter at $x = 0.3$ plotted in the $\rho - T$ plane.

- [31] D. Frenkel and B. Smit, *Understanding Molecular Simulation* (Academic Press, London, 1996).
- [32] S. Nosé, *J. Chem. Phys.* **81**, 511 (1984).
- [33] W. G. Hoover, *Phys. Rev. A* **31**, 1695 (1985).
- [34] K. Michielsen and H. De Raedt, *Phys. Rep.* **347**, 461 (2001).
- [35] J. Schmalzing, S. Engineer, T. Buchert, V. Sahni and S. Shandarin, (1996) unpublished.
- [36] J. R. Gott III, A. L. Melott and M. Dickinson, *Astrophys. J.* **306**, 341 (1986); D. H. Weinberg, *Publ. Astron. Soc. Pacific* **100**, 1373 (1988).
- [37] In the present simulations, thermal fluctuations with a wavelength longer than the box size cannot be incorporated. We should remark that these modes could be effective at destroying the long-range order of the phase with slablike nuclei.
- [38] The phase diagram for $x = 0.5$ in Fig. 18 is slightly modified several points from Fig. 1 in G. Watanabe, K. Sato, K. Yasuoka and T. Ebisuzaki, astro-ph/0310290, to appear in “Young Neutron Stars and Their Environments” (IAU Symposium 218, ASP Conference Proceedings), eds F. Camilo and B. M. Gaensler.
- [39] C. J. Pethick and A.Y. Potekhin, *Phys. Lett.* **B427**, 7 (1998).

This figure "fig1.jpg" is available in "jpg" format from:

<http://arxiv.org/ps/nucl-th/0311083v1>

This figure "fig2.jpg" is available in "jpg" format from:

<http://arxiv.org/ps/nucl-th/0311083v1>

This figure "fig3.jpg" is available in "jpg" format from:

<http://arxiv.org/ps/nucl-th/0311083v1>

This figure "fig4.jpg" is available in "jpg" format from:

<http://arxiv.org/ps/nucl-th/0311083v1>

This figure "fig5.jpg" is available in "jpg" format from:

<http://arxiv.org/ps/nucl-th/0311083v1>

This figure "fig8.jpg" is available in "jpg" format from:

<http://arxiv.org/ps/nucl-th/0311083v1>

This figure "fig9.jpg" is available in "jpg" format from:

<http://arxiv.org/ps/nucl-th/0311083v1>